Journal of Materials Chemistry

Cite this: J. Mater. Chem., 2012, 22, 2658

www.rsc.org/materials

PAPER

Synthesis and characterisation of vanadium doped alkaline earth lanthanum germanate oxyapatite electrolyte†

Henan Li,[a] Tom Baikie,[a] Stevin S. Pramana,[a] J. Felix Shin,[b] Peter R. Slater,[b] Frank Brink,[c] James Hester,[d] Kia Wallwork[e] and Tim J. White*[ac]

Received 4th August 2011, Accepted 19th November 2011
DOI: 10.1039/c1jm13752b

The crystal chemistry and oxygen conductivity of vanadium-doped apatites of nominal composition $[La_8AE_2][Ge_{6-x}V_x]O_{26+x/2}$ (AE = Ca, Sr, Ba; $0 \leq x \leq 1.5$) were studied to establish their potential as intermediate temperature solid oxide fuel cell (SOFC) electrolytes. Single-phase products obtained for $x \leq 0.5$ were found, using a combination of powder synchrotron X-ray and neutron diffraction, to be $P6_3/m$ apatites. The ionic conductivities extracted by complex impedance spectroscopy showed that small vanadium amendments enhanced oxygen mobility at intermediate temperatures (500–700 °C) by more than one order of magnitude, as the incorporation of V^{5+} through displacement of Ge^{4+} is charge balanced with interstitial O^{2-} that improves ionic conduction. The most promising composition was $La_{7.88}Ca_2Ge_{5.35}V_{0.65}O_{26.15}$ that delivered $\sigma = 3.44 \times 10^{-4}$ S cm^{-1} at 500 °C. The superstoichiometric oxygen was delocalised, without fixed X-ray or neutron scattering centres. Crystal chemistry systematics demonstrate that the Ca-apatite was superior because the relatively small framework expanded the tunnel through reduced (La/AE)O_6 metaprism twisting (φ), ensuring the $P6_3/m$ symmetry was adopted, which favours the passage of O^{2-} with lower activation energy.

1. Introduction

Oxide ion conductors have attracted widespread interest, especially as electrolytes in solid oxide fuel cells (SOFCs). High oxide ion mobility at intermediate temperatures (500–700 °C) has been observed in non-stoichiometric $[A^I_4][A^{II}_6][(BO_4)_6]O_2$ apatite-type rare earth silicates by Nakayama *et al.*,[1–3] triggering ongoing investigation of the synthesis, structure, and conductivity of these materials.[4–28] Contrary to the traditional fluorite-type or perovskite-type oxides, where oxide ions are transported *via* a vacancy mechanism achieved through specific cation doping,[11] migration in apatite-type silicates/germanates, prototypically $La_{9.33}(Si/Ge)_6O_{26}$, is often mediated by the creation of oxygen interstitials.[25,28–31] Apatites contain several cation acceptor sites leading to a wide range of substitutional possibilities[24] with ion mobility modified by varying cation type and proportions. Extensive studies of the factors influencing electrolyte performance have appeared, which show that cation-deficient or oxygen excess systems deliver higher conductivity than stoichiometric compositions. Specifically, pentavalent element doping can be used to inject superstoichiometric oxygen as attempted in vanadium doped silicate apatites.[32–34] Here, we targeted vanadium-substituted germanate oxyapatites with fully occupied cation sites $[La_8AE_2][Ge_{6-x}V_x]O_{26+x/2}$ (AE = Ca, Sr, Ba; $0 \leq x \leq 1.5$) to assess the impact of a high-valency ion (V^{5+}) on functionality, search for interstitial oxygen, and identify those factors which enhance electrolyte conductivity.

2. Experimental methods

2.1 Synthesis

Electrolyte apatites of nominal composition $[La_8AE_2][Ge_{6-x}V_x]O_{26+x/2}$ (AE = Ca, Sr, Ba; $0 \leq x \leq 1.5$) were prepared by solid-state synthesis using stoichiometric quantities of oxides and carbonates: La_2O_3 (Aldrich, 99.9%), GeO_2 (Alfa, 99.999%), $SrCO_3$ (BDH, 98.5%), $BaCO_3$ (Fluka, 98.5%), $CaCO_3$ (Kanto, 99.5%), and V_2O_5 (Fluka, 98%). Lanthanum oxide was pre-calcined at 1000 °C for 4 h to ensure dehydration and decarbonation, while germanium oxide and the carbonates were treated at 600 °C and 500 °C, respectively. The oxide and

[a]Nanyang Technological University, School of Materials Science and Engineering, 50 Nanyang Avenue, 639798, Singapore. E-mail: lihe0008@e.ntu.edu.sg; Fax: +65 6790 9081; Tel: +65 6790 4586
[b]School of Chemistry, University of Birmingham, Edgbaston, Birmingham, B15 2TT, UK. Tel: +44 (0)121 414 8906
[c]Centre for Advanced Microscopy, The Australian National University, R N Robertson Building (Bldg 46), Sullivan's Creek Road, Canberra, ACT 0200, Australia. Tel: +61 (0)2 6125 6883
[d]Australian Nuclear Science and Technology Organisation (ANSTO), New Illawarra Road, Lucas Heights, NSW, Australia. Tel: +61 (0)2 9717 9907
[e]Australian Synchrotron Company Ltd, 800 Blackburn Rd, Clayton, VIC 3168, Australia. Tel: +61 (0)3 8540 4162

† Electronic supplementary information (ESI) available. CCDC reference numbers [CCDC NUMBER(S)]. For ESI and crystallographic data in CIF or other electronic format see DOI: 10.1039/c1jm13752b

carbonate reactants were manually ground for 20 minutes with an agate mortar and pestle, and calcined in air for two cycles (1300 °C/16 h followed by 1350 °C/16 h) with intermediate regrinding. The overall ideal reaction is

$$4La_2O_3 + 2AECO_3 + (6 - x)GeO_2 + (x/2)V_2O_5 \rightarrow La_8AE_2\text{-}Ge_{6-x}V_xO_{26+x/2} + 2CO_2\uparrow \quad (1)$$

where $x = 0.0$, 0.25, 0.5, 0.75, 1.0, 1.25, and 1.5.

2.2 Powder diffraction

For the electrolyte compositions considered here, it was essential to combine X-ray and neutron diffraction to arrive at complete crystallographic descriptions. Specifically, X-ray methods are unable to differentiate La from Ba, and the form factors for V and Ge are similar. On the other hand, neutrons are essential to derive oxygen positions, but lack the sensitivity to distinguish Sr from La, and V cannot be detected directly.

Laboratory powder X-ray diffraction (XRD) patterns were acquired at room temperature using a Bruker D8 Advance diffractometer fitted with a LynxEye silicon strip detector, and using CuK_α (λ_{av} = 1.54056Å) radiation, coupled θ–2θ geometry over the angular range 10° < 2θ < 130°, and a step size of 0.02° with a counting time of 1 s per step.

High resolution synchrotron powder X-ray diffraction patterns were collected from $[La_8(Ca/Sr/Ba)_2][Ge_{6-x}V_x]O_{26+x/2}$ ($0 \leq x \leq 1.5$) at room temperature using the Powder Diffraction Beamline at the Australian Synchrotron Light Source fitted with a Si (111) double crystal monochromator (DCM). A wavelength of 0.61885Å (20.0349 keV) was selected to avoid absorption edges and secondary fluorescence, and probe a large volume of reciprocal space. The apatites were mixed with 20 wt% CaF_2 as an internal calibrant of peak position and intensity (a = 5.47093Å, space group $Fm\bar{3}m$), and loaded into 0.3 mm diameter low X-ray absorption soda lime glass capillaries that were rotated during the experiment. Patterns were accumulated at a step size of 0.00375° over the angular range 5–66.6° 2θ.

Neutron powder diffraction data were gathered from $[La_8(Ca/Sr/Ba)_2][Ge_{6-x}V_x]O_{26+x/2}$ (x = 0, 0.25 and 0.5) using the Echidna (high resolution powder diffractometer) beamline at ANSTO (Australian Nuclear Science and Technology Organisation) drawing neutrons from the Open Pool Australian Lightwater (OPAL) reactor. A Ge (335) monochromator with 140° take-off angle yielded a neutron wavelength of 1.622Å. Vanadium cans (10 mm in diameter) contained the samples and 25 datasets of unique composition were collected at ambient temperature over the range of 4–164° 2θ with a step size of 0.05° for 3 h.

2.3 Rietveld refinement procedures and strategies

For both synchrotron and neutron powder X-ray diffraction data, Rietveld analysis of $[La_8AE_2][Ge_{6-x}V_x]O_{26+x/2}$ was conducted using *TOPAS*.[35] A pseudo-Voigt peak shape function modelled the Bragg reflections using $La_{9.33}Ge_6O_{26}$ ($P6_3/m$) as the starting structure.[6] A four-coefficient Chebychev polynomial and $1/x$ profile background, a zero error, scale factors, and lattice dimensions were refined sequentially. [La/*AE*] and [Ge/V] occupancies were refined, followed by atom positions and isotropic atomic displacement parameters (ADPs) in groups as follows: framework A^I cations; tunnel A^{II} cations; Ge; and all oxygen (framework, tunnel, and interstitial). Anisotropic atomic displacement factors were refined for oxygen only using the neutron diffraction patterns.

Initially, full site occupancies were assumed for all atomic sites, but this approach always resulted in an overall alkaline earth dopant *AE* (Ca, Sr, or Ba) stoichiometry larger than expected (*i.e.* >2 atoms per formula unit (apfu)). As earlier studies suggested the involvement of A^I 4*f* vacancies,[36] the refinement strategy was modified to allow for framework substoichiometry and ensure the large cation content ($A^I + A^{II}$) agreed with the nominal synthetic composition. The La/*AE* occupancies on the A^{II} 6*h* site were fixed at 6 apfu as there are no reports of vacancies at this position, and the number of *AE* atoms on the A^I site calculated (=2 − alkaline earth on the A^{II} site) and fixed. Finally, the La occupancy on the A^I site was released without any constraint. In this manner, the sum of $A^I + A^{II}$ cations is always equal to or less than 10 apfu within error, and the number of vacancies can be determined (=10 − total cations on the *A* sites).

As noted, the relative occupancies La/Sr derived from neutron data are unreliable because of the similar bound coherent scattering lengths (La : Sr = 8.24 fm : 7.02 fm).[37] Similarly, La/Ba occupancies from synchrotron refinement are imprecise because of the close atomic numbers (La : Ba = 57 : 56). The X-ray scattering power on the *B* site is only slightly changed by minor (0.5 apfu) vanadium replacement of germanium. On the other hand, for neutron diffraction, the Ge/V scattering lengths are quite different (8.185 fm : −0.3824 fm),[37] although the determination is indirect, since the coherent neutron scattering length of vanadium is extremely low and the V occupancy is inferred from the reduction in scattering at the Ge/V sites.

To exploit these diffraction characteristics, a refinement strategy that combined the merits of both techniques was devised (Fig. S1†). (i) For the Ca series, the synchrotron refinements took the Ge/V ratio derived from neutron diffraction. (ii) For the Sr series, Ge/V occupancies were taken from the neutron data and fixed, while the La/Sr occupancies were refined from the synchrotron pattern. This process of establishing Ge/V and La/Sr ratios from neutron and synchrotron refinements was cycled until stable occupancies were reached. (iii) For the Ba series, both La/Ba and Ge/V occupancies in synchrotron refinements were fixed at values derived from neutron diffraction.

While in principle a joint refinement of synchrotron X-ray and neutron data should be feasible, attempts to conduct the refinements in this fashion were unsuccessful. The poor convergence is attributed to the vastly different intensity of the two patterns (Fig. 1) with the X-ray counts dominating the minimization, leading to non-physical crystallographic parameters.

2.4 Scanning and transmission electron microscopy

For scanning electron microscopy (SEM) the powdered samples were prepared by embedding them in epoxy resin disks (diameter 25 mm and thickness 5 mm), followed by polishing to a <1 μm finish. Backscattered electron (BSE) images were collected using a JEOL JSM 6400 and JEOL JSM 7600F. Electron probe microanalysis was performed on each of the samples to confirm the actual composition. The quantitative analyses were carried out at 15 kV and 1 nA using a JEOL JSM 6400 SEM equipped

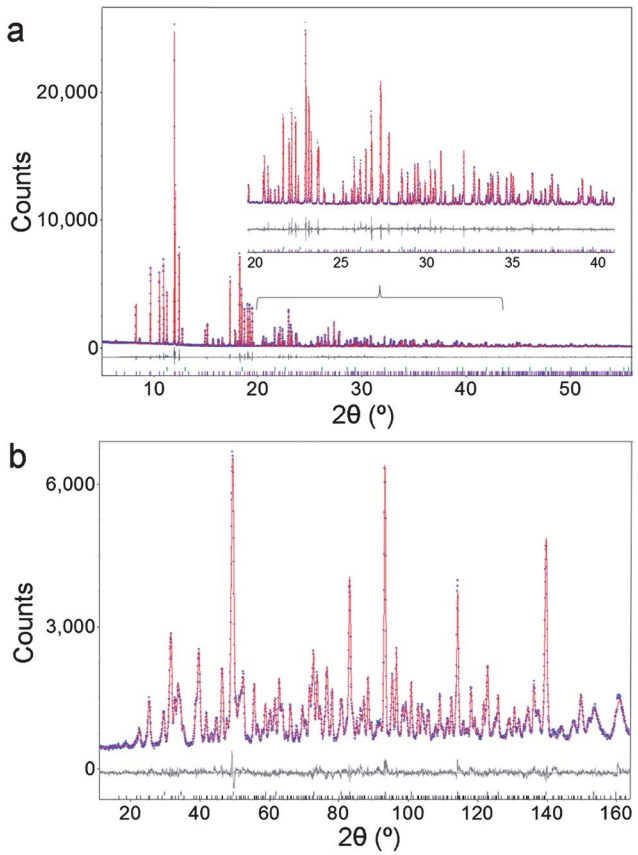

Fig. 1 Rietveld plots of the (a) synchrotron and (b) neutron powder diffraction data of nominal $La_8Sr_2Ge_{5.5}V_{0.5}O_{26.25}$ collected at room temperature. The observed intensity is shown by dots, with the solid line representing the calculated intensity. Differences between observed and calculated intensities are plotted beneath. Vertical markers indicate the Bragg reflections of CaF_2 standard (top) and apatite (bottom).

with an Oxford Instruments light element EDS detector and Link ISIS SEMquant software. Pure V and the end member $La_8Sr_2Ge_6O_{26}$ were used as calibration reference standards throughout. A Zeiss UltraPlus Field Emission Scanning Electron Microscope (FESEM) equipped with an HKL electron backscatter diffraction (EBSD) system was used to examine the crystal texture of the sintered pellet for $La_8Ba_2Ge_{5.5}V_{0.5}O_{26.25}$. For transmission electron microscopy (TEM) the apatites were finely ground under ethanol, then ultrasonically dispersed for ~10 min. Several drops of the suspension were deposited on a holey carbon film supported by a copper grid that was dried before introduction to the microscope. High-resolution (HR) images and selected area electron diffraction (SAED) patterns were collected using a JEOL JEM-2010 TEM at 200 keV.

2.5 Raman and Fourier transform infrared spectroscopy

All infrared spectroscopy was conducted at room temperature. The Raman spectra were collected in a WITec CRM200 confocal Raman microscopy system (laser wavelength 488 nm and spot size ~0.5 μm), with the Si band at 520 cm^{-1} used for wavenumber calibration. Fourier transform infrared (FTIR) spectra were gathered from 400 and 4000 cm^{-1} using a Perkin Elmer (Spectrum 2000) spectrophotometer with a spectral resolution of 4 cm^{-1}. Translucent pellets were prepared by mixing and pelletising apatite powder with oven-dried (120 °C) potassium bromide (KBr). FTIR is complementary to Raman spectroscopy for qualitative confirmation of vanadium incorporation, but assignment of specific Ge–O and V–O absorption bands was not possible due to the extensive convolutions from 580–1000 cm^{-1}.

2.6 Impedance spectroscopy

Compact pellets (1.0 cm diameter) for conductivity measurements were prepared as follows: the apatite powders were mixed with binder (isopropyl alcohol with 3% polyvinyl butyral), pelletised (300 bar) uniaxially, and sintered at 1500 °C for six hours. Both sides of the pellets were coated with Au paste and then heated to 750 °C to ensure bonding to the pellet. The ionic conductivity was then studied by alternating current (AC) impedance spectroscopy (Hewlett Packard 4182A impedance analyser). The measurements were taken in air at an applied voltage of 0.1 V over a frequency range of 100 Hz to 10 MHz from 300 to 800 °C.

3. Results

3.1 Phase assemblage and lattice metric

Laboratory powder X-ray diffraction patterns confirmed the synthesis of single phase, crystalline products for the Ca, Sr, and Ba substituted $[La_8AE_2][Ge_{6-x}V_x]O_{26+x/2}$ series with nominal compositions $0 \leq x \leq 0.5$ (Fig. 2 and S2†). Beyond $x = 0.5$, secondary phases appeared that could not be identified against known compounds and became more abundant as the vanadium content increased. Consequently, the balance of these studies focussed on $x \leq 0.5$ preparations.

Although germanium volatilisation has been reported when firing at 1500 °C[21]or at 1300 °C[38] for long periods (120 h), losses here were not significant under the relatively mild and short firing time used. Moreover, energy dispersive X-ray microanalysis (Table S1†) and diffraction did not detect secondary phases or

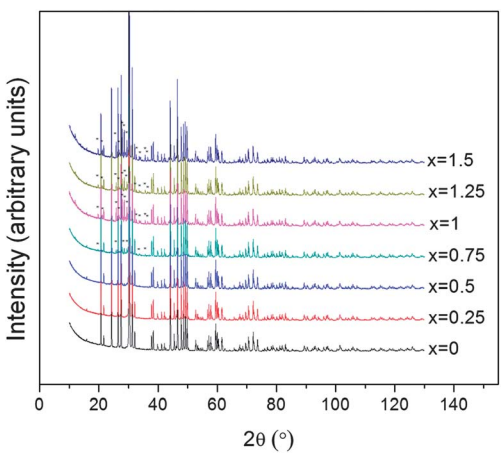

Fig. 2 PXRD data for $[La_8Sr_2][Ge_{6-x}V_x]O_{26+x/2}$ series with $x = 0$, 0.25, 0.5, 0.75, 1, 1.25, and 1.5 synthesised with two calcination cycles at 1300 and 1350 °C for 16 hours separately. Under these preparative conditions the solid-solution limit is $x = 0.5$. For $x > 0.5$, peaks from secondary phases are labelled with *.

Table 1 Refined crystal and atomic parameters from synchrotron powder X-ray diffraction of $La_8Sr_2Ge_{6-x}V_xO_{26+x/2}$ ($x = 0$, 0.25, and 0.5)

Nominal x	0	0.25	0.5
Refined composition	$La_{7.93}Sr_2Ge_6O_{25.90}$	$La_{7.93}Sr_2Ge_{5.84}V_{0.16}O_{25.98}$	$La_{7.99}Sr_2Ge_{5.58}V_{0.42}O_{26.20}$
R_{exp} (%)	2.29	2.30	2.39
R_{wp} (%)	4.48	4.88	7.71
R_p (%)	3.29	3.57	5.32
R_b (%)	1.48	1.56	2.10
GOF	1.95	2.12	3.23
Amorphous phase[a] (wt%)	7.3(5)	13.6(5)	15.6(7)
Apatite[a] (wt%)	92.70(10)	86.38(12)	84.44(17)
a/Å	9.920979(14)	9.920248(14)	9.92016(2)
c/Å	7.329844(14)	7.331756(14)	7.33324(2)
V/Å^3	624.791(2)	624.861(2)	624.977(3)
c/a	0.7388	0.7391	0.7392
Twist angle φ/°	24.2_6	23.8_4	24.4_4
La/Sr(1), 4f, (1/3 2/3 z)			
z	0.00039(13)	0.00039(14)	−0.0001(2)
B/Å^2	0.329(10)	0.483(12)	0.48(2)
Occ La/Sr(1)	0.561(4)/0.422(7)	0.534(5)/0.449(8)	0.511(8)/0.486(13)
La/Sr(2), 6h, (x y 1/4)			
x	0.23036(4)	0.23002(5)	0.22942(8)
y	−0.01099(6)	−0.01127(6)	−0.01159(10)
B/Å^2	0.106(7)	0.183(7)	0.223(12)
Occ La/Sr(2)	0.948(5)/0.052(5)	0.966(5)/0.034(5)	0.991(9)/0.009(9)
Ge/V, 6h, (x y 1/4)			
x	0.39966(7)	0.39950(8)	0.39904(12)
y	0.37198(7)	0.37213(8)	0.37206(13)
B/Å^2	0.097(13)	0.158(15)	0.03(3)
Occ Ge/V[b]	1.00/0.00	0.9741/0.0259	0.9308/0.0692
O(1), 6h, (x y 1/4)			
x	0.3116(5)	0.3125(5)	0.3114(8)
y	0.4859(5)	0.4848(5)	0.4839(8)
B/Å^2	0.55(8)	0.55(9)	0.50(15)
O(2), 6h, (x y 1/4)			
x	0.6011(5)	0.6017(5)	0.6003(8)
y	0.4759(5)	0.4757(5)	0.4756(8)
B/Å^2	0.42(8)	0.67(9)	0.19(13)
O(3), 12i, (x y z)			
x	0.3396(3)	0.3397(4)	0.3395(6)
y	0.2486(3)	0.2481(4)	0.2491(6)
z	0.0630(4)	0.0639(4)	0.0642(7)
B/Å^2	1.03(7)	1.31(8)	1.60(13)
O(4), 2a, (0 0 1/4)			
B/Å^2	1.30(13)	1.37(15)	2.0(3)

[a] Spiked with 20 wt% CaF_2 standard. [b] The occupancies for Ge and V were fixed to values derived from neutron diffraction.

departures from expected compositions. Further, the introduction of vanadium oxide reduces the apatite crystallisation temperature, thereby suppressing evaporative loss of germanium.

Rietveld quantitative phase analysis (QPA) of both synchrotron and neutron powder diffraction data (Tables 1–3, S2–S8†) confirmed apatite and the calcium fluoride internal standard, however, the apparent fluoride content derived from X-ray patterns exceeds the weighted 20 wt%. This can be attributed to a co-existing non-diffracting component, but represents a substantial overestimate due to the influence of X-ray micro-absorption,[39] especially for vanadium-rich materials where crystal sizes are larger (see Section 3.3). In contrast, neutron QPA is reliable and shows that within error, fully crystalline products were achieved, with only the possibility of minor glassy phases at grain boundaries. The refined unit cell constants (a, c, and c/a) from synchrotron powder X-ray diffraction of $[La_8AE_2][Ge_{6-x}V_x]O_{26+x/2}$ (nominal $x = 0$, 0.25, and 0.5) (Fig. 3) found that Ba apatites have the largest lattice metric compared to the intermediate Sr analogues and the smallest Ca series, as expected due to the ascending ionic radii of the framework cations: Ca^{2+} (CN 8, 1.12Å) < Sr^{2+} (CN 8, 1.26Å) < Ba^{2+} (CN 8, 1.42Å).[40] Within the same alkali-earth series, the lattice parameters are without obvious trend with increasing x, because Ge^{4+} and V^{5+} are of similar size (Ge^{4+} (CN 4) = 0.39Å; V^{5+} (CN 4) = 0.36Å).[40] However, in plots with expanded scales (Fig. S3†), a and c are seen to react oppositely, but slightly, with increasing V^{5+} content. In general, a contracts while c expands, such that the unit cell volume is essentially constant.

3.2 Crystal structures

Rietveld crystal structure refinement of $[La_8AE_2][Ge_{6-x}V_x]O_{26+x/2}$ (nominal $x = 0$, 0.25 and 0.5) in hexagonal $P6_3/m$ for synchrotron and neutron data yielded good agreement between calculated and observed patterns (Tables 1–3 and S2–S8†, and Fig. 1). In every

Table 2 Refined crystal and atomic parameters from neutron powder diffraction of $La_8Sr_2Ge_{6-x}V_xO_{26+x/2}$ ($x = 0$, 0.25, and 0.5)

Nominal x	0	0.25	0.5
Refined composition	$La_{7.93}Sr_2Ge_6O_{25.90}$	$La_{7.93}Sr_2Ge_{5.84}V_{0.16}O_{25.98}$	$La_{7.99}Sr_2Ge_{5.58}V_{0.42}O_{26.20}$
R_{exp} (%)	3.06	3.04	3.06
R_{wp} (%)	4.36	4.22	4.40
R_p (%)	3.48	3.38	3.52
R_b (%)	1.73	1.65	1.65
GOF	1.42	1.39	1.44
Amorphous phase[a] (wt%)	2.9(9)	2.1(10)	1.5(10)
Apatite[a] (wt%)	97.1(2)	97.9(2)	98.5(2)
a/Å	9.91022(13)	9.90847(18)	9.90941(13)
c/Å	7.32094(14)	7.32192(16)	7.32414(15)
V/Å^3	622.68(2)	622.54(3)	622.85(2)
c/a	0.7387	0.7390	0.7391
Twist angle φ/°	23.5_8	23.9_9	24.2_4
La/Sr(1), 4f, (1/3 2/3 z)			
z	0.4980(5)	0.4984(5)	0.4977(5)
Occ La/Sr(1)[b]	0.5611/0.4217	0.5337/0.4490	0.5112/0.4860
La/Sr(2), 6h, (x y 1/4)			
x	0.2309(2)	0.2311(2)	0.2304(2)
y	−0.0094(3)	−0.0095(3)	−0.0096(3)
Occ La/Sr(2)[b]	0.9478/0.0522	0.9660/0.0340	0.9906/0.0094
Ge/V, 6h, (x y 1/4)			
x	0.4003(3)	0.3999(3)	0.3993(3)
y	0.3724(2)	0.3723(2)	0.3723(2)
Occ Ge/V	1.00/0.00	0.974(7)/0.026(7)	0.931(7)/0.069(7)
O(1), 6h, (x y 1/4)			
x	0.3118(4)	0.3103(4)	0.3098(4)
y	0.4861(4)	0.4848(4)	0.4846(4)
O(2), 6h, (x y 1/4)			
x	0.6038(3)	0.6037(3)	0.6035(3)
y	0.4765(4)	0.4767(3)	0.4761(4)
O(3), 12i, (x y z)			
x	0.3396(3)	0.3390(3)	0.3393(3)
y	0.2471(3)	0.2465(3)	0.2469(3)
z	0.0628(3)	0.0636(3)	0.0640(3)
O(4), 2a, (0 0 1/4)			

[a] Spiked with 20 wt% CaF_2 standard. [b] The occupancies for La and Sr were fixed to values derived from synchrotron diffraction.

case, the X-ray diffraction analysis found that most, if not all, of the alkaline earths (Ca/Sr/Ba) reside on the 4*f* framework sites in agreement with previous work.[5,25,41] The type of nonstoichiometry was distinct however: the Sr series was negligibly substoichiometric on the A^1 (4*f*) site (less than 2% vacant), while for the Ca and Ba analogues, A^1 was 3–8% under-occupied, leading in some cases to oxygen-deficient (<26 oxygen apfu) compositions with partial occupancy of the tunnel 2*a* anion position; this is especially evident for Ba of nominal $x = 0.5$. Mechanisms for the incorporation of vanadium, cation vacancies, and oxygen interstitials can be collated as:

$$2Ge^{4+} + \square_{Oi} \rightarrow 2V^{5+} + O^{2-} \quad (2)$$

$$2La^{3+} + 3O^{2-} \rightarrow 2\square_{La}{}^{3+} + 3\square_{O}{}^{2-} \quad (3)$$

A general scheme that includes eqn (2) and (3) can be written as:

$$2xGe^{4+} + 2yLa^{3+} + x\square_{Oi} \rightarrow 2xV^{5+} + 2y\square_{La}{}^{3+} + 3y\square_{O}{}^{2-} + (x - 3y)O^{2-} \quad (4)$$

A further mechanism, believed to be less significant, may be:

$$2La^{3+} + O^{2-} \rightarrow 2AE^{2+} + \square_{O}{}^{2-} \quad (5)$$

Although the incorporation of vanadium ions into apatite should introduce excess oxygen *via* mechanism (2), the lack of direct diffraction evidence for an interstitial oxygen site in the hexagonal channel or elsewhere suggests that charge balance arises primarily by the creation of La^{3+} vacancies (mechanism (3)), or more likely, the extra oxygen is delocalised and does not contribute to Bragg diffraction of neutrons as suggested by Beaudet-Savignat *et al.*[5] It is noted that the oxide ions in the channel have large [001] anisotropic displacements for all compositions, as would be expected if static disorder (mechanism (2)) is operative. In practice, the combined mechanism (4) will be active, though the x and y proportions will be specific for the stoichiometry and firing temperature. The refined vanadium content x for Sr series is smaller than those for Ca and Ba analogues, because the A^1 site vacancies for the latter series exceed those for the Sr series, as follows (nominal $x = 0.5$, ratios were derived from Rietveld refined neutron diffraction patterns):

$$\text{Ca: } 0.65Ge^{4+} + 0.11La^{3+} + 0.16\square_{Oi} \rightarrow 0.65V^{5+} + 0.11\square_{La}{}^{3+} + 0.16O^{2-} \quad (6)$$

$$\text{Sr: } 0.42Ge^{4+} + 0.01La^{3+} + 0.20\square_{Oi} \rightarrow 0.42V^{5+} + 0.01\square_{La}{}^{3+} + 0.20O^{2-} \quad (7)$$

Table 3 Isotropic and anisotropic displacement parameters refined from neutron powder diffraction for $La_8Sr_2Ge_{6-x}V_xO_{26+x/2}$ ($x = 0$, 0.25, and 0.5)

Nominal x	0	0.25	0.5
Refined composition	$La_{7.93}Sr_2Ge_6O_{25.90}$	$La_{7.93}Sr_2Ge_{5.84}V_{0.16}O_{25.98}$	$La_{7.99}Sr_2Ge_{5.58}V_{0.42}O_{26.20}$
La/Sr(1), 4f, (1/3 2/3 z)			
B/Å^2	0.46(4)	0.46(4)	0.46(4)
La/Sr(2), 6h, (x y 1/4)			
B/Å^2	0.32(3)	0.27(3)	0.31(3)
Ge/V, 6h, (x y 1/4)			
B/Å^2	0.51(4)	0.55(5)	0.49(5)
O(1), 6h, (x y 1/4)			
U_{11}	0.0196(17)	0.0180(16)	0.0161(17)
U_{22}	0.0084(16)	0.0125(17)	0.0102(18)
U_{33}	0.0086(15)	0.0071(15)	0.0064(16)
U_{12}	0.0112(15)	0.0134(15)	0.0117(15)
$U_{13} = U_{23} = 0$			
O(2), 6h, (x y 1/4)			
U_{11}	0.0068(15)	0.0037(14)	0.0044(15)
U_{22}	0.0094(15)	0.0069(14)	0.0047(15)
U_{33}	0.0098(16)	0.0134(16)	0.0129(17)
U_{12}	0.0013(13)	−0.0008(12)	−0.0015(13)
$U_{13} = U_{23} = 0$			
O(3), 12i, (x y z)			
U_{11}	0.0318(18)	0.0371(18)	0.0392(19)
U_{22}	0.0158(13)	0.0138(12)	0.0110(12)
U_{33}	0.0101(10)	0.0090(10)	0.0107(10)
U_{12}	0.0126(11)	0.0152(11)	0.0160(11)
U_{13}	−0.0112(10)	−0.0097(10)	−0.0104(11)
U_{23}	−0.0037(9)	−0.0030(9)	−0.0019(9)
O(4), 2a, (0 0 1/4)			
U_{11}	0.0191(17)	0.0145(16)	0.0139(17)
U_{22}	0.0191(17)	0.0145(16)	0.0139(17)
U_{33}	0.024(3)	0.021(3)	0.022(3)
U_{12}	0.0095(9)	0.0073(8)	0.0069(9)
$U_{13} = U_{23} = 0$			

$$\text{Ba: } 0.71Ge^{4+} + 0.33La^{3+} + 0.14O^{2-} \rightarrow 0.71V^{5+} + 0.33\square_{La}{}^{3+} + 0.14\square_{O}{}^{2-} \quad (8)$$

Mismatch between the flexible framework and tunnel ions distorts the structure through $A^{I}O_6$ metaprism twisting (counter-rotation of the opposing triangular faces of the metaprism through a [001] projected angle), with the twist angles (φ) calculated from neutron diffraction refinements providing superior reliability of oxygen positions (Fig. 4a). As anticipated, the twist angles follow the trend Ba > Sr > Ca (Fig. 4b) because the alkaline earths primarily occupy the framework and control the tunnel diameter. Consequently, when Ba is accommodated in the $A^{I}O_6$ metaprism, this polyhedron must have a large φ (~25°) to constrict the framework around the relatively small tunnel contents ($La^{II}{}_6O_2$). At the other extreme, Ca insertion reduces framework polyhedra volumes, and so φ (~21.5°) must become more acute to open the channel sufficiently to satisfy bonding to its contents. Being of intermediate size, Sr analogues show $\varphi \approx 24°$.

The trends for any given alkaline earth series as a function of V^{5+} content (x) are subtle, as V^{5+} and Ge^{4+} are of similar size, and because the relative importance of substitution mechanisms (2) and (3) will vary. As V^{5+} is slightly smaller than Ge^{4+}, increasing x reduces framework size and φ is more acute. The trends for all three series result from the combined effects of varying A^{I}/A^{II} size ratios, A^{I} site vacancy concentrations, and the extent of vanadium substitution (Fig. 4c).

3.3 Microstructure and local structure

The BSE micrographs for the $[La_8Sr_2][Ge_{6-x}V_x]O_{26+x/2}$ series show homogeneous contrast for single-phase apatites ($x \leq 0.5$), but for $x > 0.5$ several distinct regions arise from the secondary phases (as also observed by XRD) (Fig. S4†). For the Sr series, the chemical compositions for $x \leq 0.5$ were probed by EDS with variance established by averaging (over 15 analyses) (Table S1†). There is an apparent deviation from the nominal compositions, which correlates well with the refined compositions from Rietveld analysis. The La content is lower than expected, which is attributed to vacancies on the A^{I} cation sites. The Ge/V ratios are close to nominal, however, the low concentration of vanadium leads to a relatively large standard deviation. For samples with $x > 0.5$, the proportion of secondary phases is significant and three compounds, in addition to apatite, were detected in the $x = 1.5$ material (Table S9†) containing an excess of La and/or V. The identity of these phases remains to be determined.

BSE images of the sintered pellets show equiaxed grains (Fig. 5a, b and d) for Ca- and Sr-substituted apatites with grain sizes ranging from 6–10 μm, while the Ba-substituted crystals are elongated along [001] (Fig. 5c) to 10 to >100 μm, which is similar to the morphology of Sr-substituted lanthanum silicate apatite.[12] Existence of intergranular material was observed (Fig. S5†), which may be glassy, as suggested earlier by neutron QPA. The obvious, complex features at some interfaces are of similar contrast and composition with the apatite phase. On the other

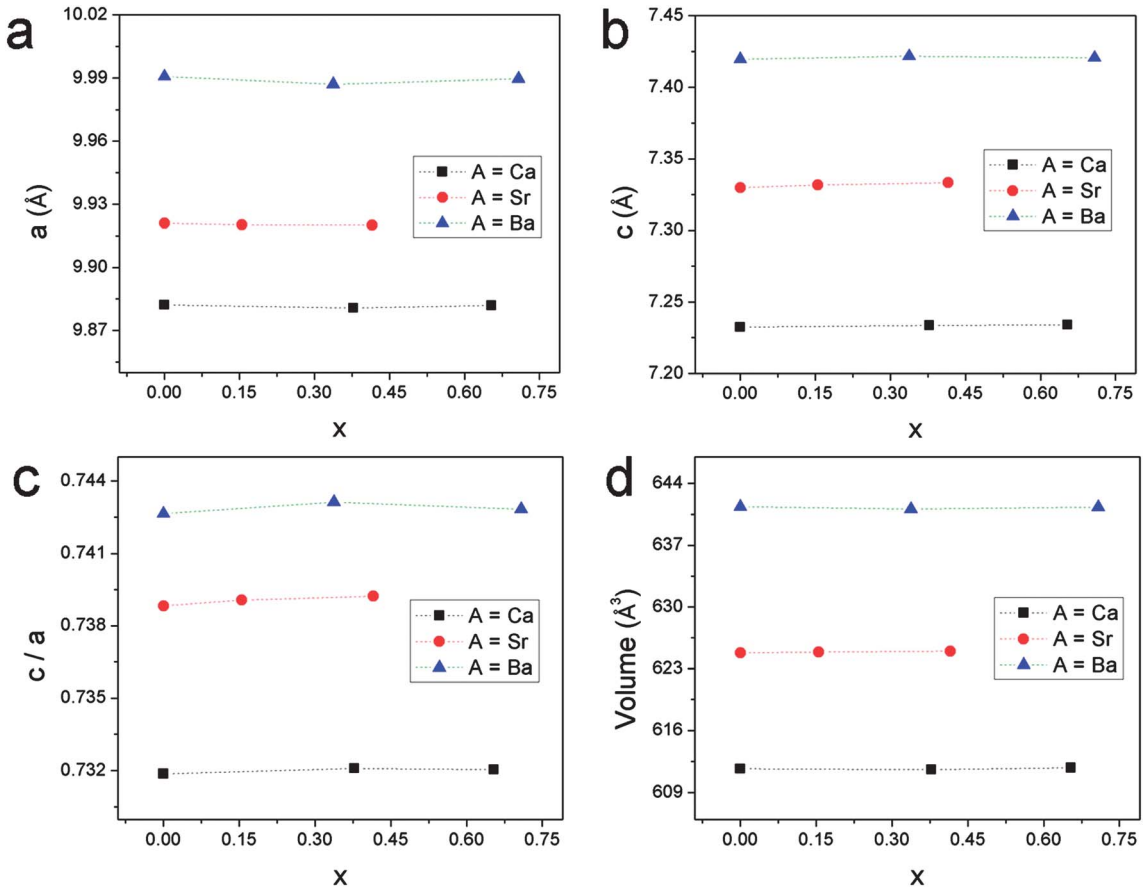

Fig. 3 Refined lattice parameters from synchrotron powder X-ray diffraction data for $La_8AE_2Ge_{6-x}V_xO_{26+x/2}$ (AE = Ca, Sr, Ba) (a) a, (b) c, (c) c/a, and (d) unit cell volume. The x-values are those derived from Rietveld analysis.

hand, the clean grain boundaries sometimes contain narrow darker contrast and are possibly germanium/vanadium rich glasses. The crystal masses are without texture, and XRD of pellet surfaces confirmed only a minor degree of (100), (011) and (210) preferred orientations (Fig. S6†). Apatite crystals become increasingly c-axis acicular with the introduction of larger alkaline earth ions (Ba^{2+} > Sr^{2+} > Ca^{2+}), because incipient melting progressively contributes to fluxing; BaO has the lowest melting point followed by SrO and CaO, and grain growth would be more rapid at near-melting eutectic temperatures.[42] Moreover, the addition of vanadium accentuates anisotropic growth (Fig. 5e and f), as V_2O_5 melts at 690 °C which is the lowest among all oxides used here. It is well known that the liquid phase formed by V_2O_5 addition drastically alters the microstructure and increases the density of sintered ceramics,[43,44] as observed here. EBSD of nominal $[La_8Ba_2][Ge_{5.5}V_{0.5}]O_{26.25}$ confirmed preferential c-axis growth (Fig. 6) with six selected grains of different orientations.

TEM imaging and diffraction of $[La_8Sr_2][Ge_{6-x}V_x]O_{26+x/2}$ with $x = 0$ (Fig. 7a and b) and $x = 0.5$ (Fig. 7c and d) were consistent with $P6_3/m$ symmetry when viewed along ⟨101⟩ and ⟨211⟩ orientations. HRTEM contrast was not uniform, especially for vanadium-rich compositions, and rapid damage under the highly energetic electron probe may arise from vanadium volatilisation.[45]

3.4 Raman and FTIR spectroscopy

Fig. 8 shows the Raman spectra for $[La_8AE_2][Ge_{6-x}V_x]O_{26+x/2}$ ($x = 0$, 0.25 and 0.5). Following Orera *et al.*[46,47] the strong band at ~340 cm^{-1} was assigned to the ν_2 symmetric bending mode of the GeO_4 tetrahedra, and those at lower energies (<300 cm^{-1}) are mainly due to the translational and librational external modes of the GeO_4 group. The bands from 400 to 500 cm^{-1} arise from the ν_4 bending modes of the GeO_4 tetrahedra, and those observed from 700 to 800 cm^{-1} correspond to the symmetric ν_1 and asymmetric ν_3 stretching modes. A shoulder at around 800–850 cm^{-1} is due to the vanadium in apatite and not unreacted V_2O_5 (Fig. S7†).[48,49] Additional features observed in the Raman spectra are substantial band broadening and shifting towards lower energies with vanadium doping, possibly indicating greater strain, as $x = 0.5$ is approaching the vanadium solid-solution limit.

The FTIR transmission spectra for $[La_8Sr_2][Ge_{6-x}V_x]O_{26+x/2}$ ($x = 0$, 0.25 and 0.5) and $[La_8AE_2][Ge_{5.5}V_{0.5}]O_{26.25}$ show a broad peak (550–950 cm^{-1}) assigned to O–Ge–O stretching and deformation modes (Fig. S8†).[21] For the vanadium-doped apatites, there is an additional shoulder at ~850 cm^{-1} assigned to a VO_4 band[50] whose intensity increases with x, which is consistent with the Raman observations. In comparing different A-cation substitutions, the GeO_4 band shifts to lower frequencies as larger

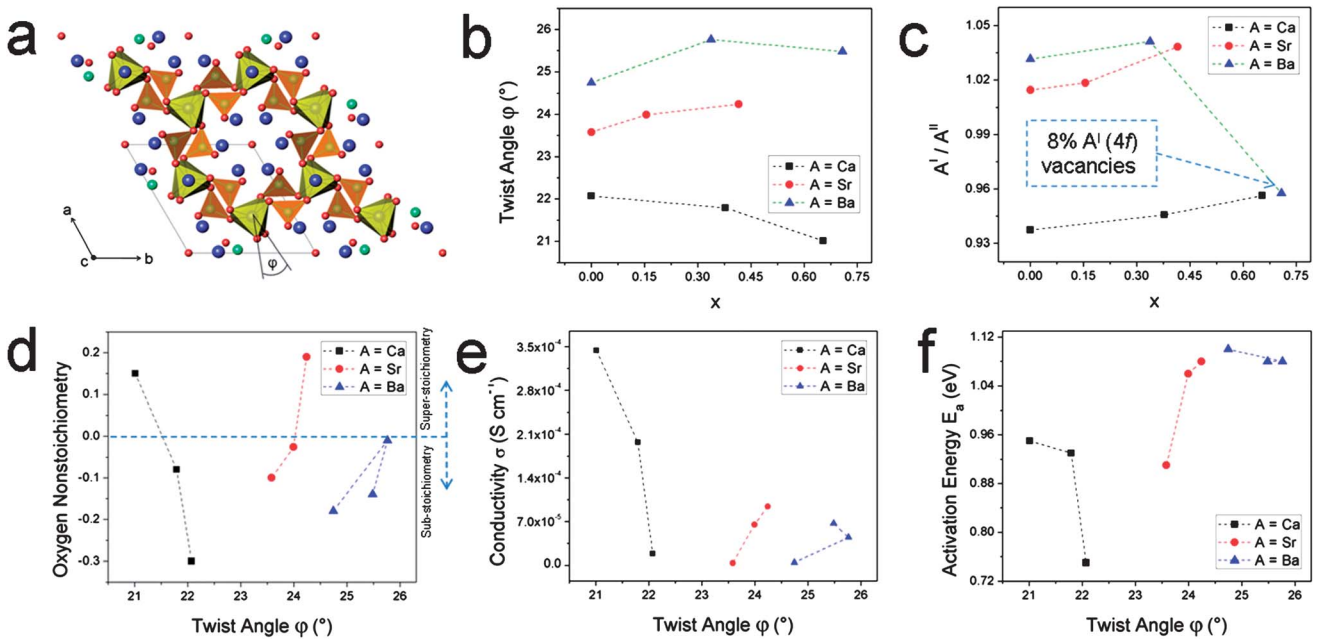

Fig. 4 Twist angle: (a) polyhedral representation of the refined $La_{7.99}Sr_2Ge_{5.58}V_{0.42}O_{26.20}$ structure with metaprism twisting (φ) labelled, face-sharing A^IO_6 metaprisms (yellow) are corner connected to BO_4 tetrahedra (orange) forming the framework, which surrounds the tunnel A^{II} atoms (blue), (b) plot of twist angles with respect to x, (c) plot of A^I/A^{II} atomic size ratio with respect to x, (d) plot of oxygen nonstoichiometry with respect to φ, (e) plot of ionic conductivity with respect to φ, and (f) plot of activation energy with respect to φ for $La_8AE_2Ge_{6-x}V_xO_{26+x/2}$ (AE = Ca, Sr, Ba).

alkali ions are incorporated. The decrease of the Ge–O vibration frequency is associated with a decrease in bond strength, accompanied by bond lengthening in the GeO_4 tetrahedra for Ca, Sr and Ba substituted apatites from 1.731Å to 1.741Å to 1.746Å, respectively, as determined by neutron diffraction.[51]

3.5 Oxide ion conductivities

The impedance data were variable, with some compositions showing a single semicircle, with a capacitance typical of a bulk response, indicating very little grain boundary contribution, while in other samples there was evidence for a second grain boundary semicircle (Fig. S9†). The conductivity data (bulk conductivities) are displayed in Fig. 9. As expected, the fully stoichiometric apatite ($La_8AE_2Ge_6O_{26}$) showed the lowest conductivity (*e.g.* AE = Sr, $\sigma = 3.53 \times 10^{-6}$ S cm^{-1}) at intermediate temperature (500 °C). However, as the oxygen content rises with the addition of vanadium (nominal $x = 0.25$), the conductivity increased by more than one order of magnitude (AE = Sr, $\sigma = 6.49 \times 10^{-5}$ S·cm^{-1}), but less obviously with further doping to $x = 0.5$ (AE= Sr, $\sigma = 9.39 \times 10^{-5}$ S·cm-1). The conductivities are comparable to those reported for equivalent apatite germanates with similar nominal oxygen excess but without doping on the Ge site (*i.e.* $La_{8.5}Ba_{1.5}Ge_6O_{26.25}$, $\sigma \approx 8 \times 10^{-5}$ S cm^{-1} at 500 °C,[52] compared to 6.68×10^{-5} S cm^{-1} for AE = Ba, $x = 0.5$), suggesting that the key influence on the conductivity is the introduction of excess oxygen

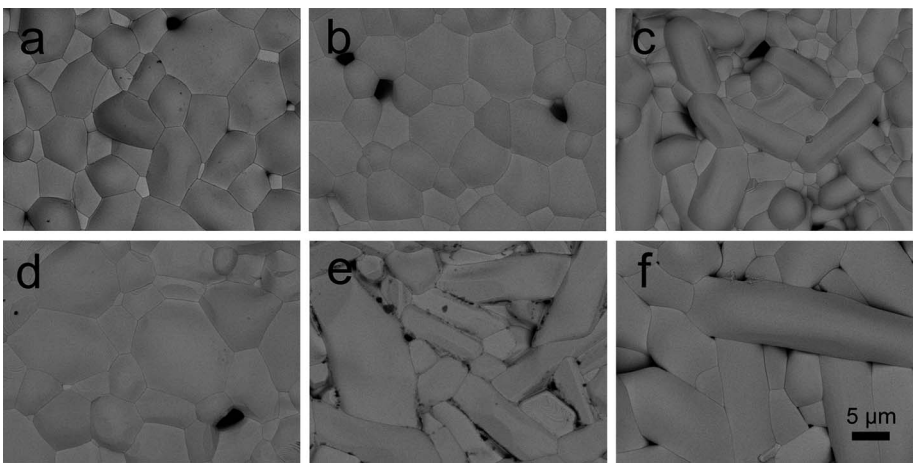

Fig. 5 Low angle backscattered electron micrographs (5.0 kV) for $[La_8AE_2][Ge_{6-x}V_x]O_{26+x/2}$ series with (a) AE = Ca, $x = 0$; (b) AE = Sr, $x = 0$; (c) AE = Ba, $x = 0$; (d) AE = Ca, $x = 0.5$; (e) AE = Sr, $x = 0.5$; and (f) AE = Ba, $x = 0.5$.

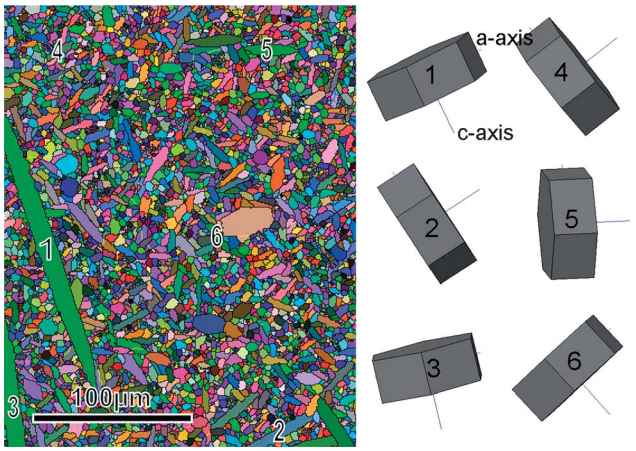

Fig. 6 EBSD analyses on polished pellet of nominal $La_8Ba_2Ge_{5.5}V_{0.5}O_{26.25}$. The all-Euler map (with grain boundaries shown by black lines) is shown on the left and crystal orientations for six elongated grains (marked on the map by numbers) are presented on the right; the growth directions of these crystals are all along the *c*-axis.

rather than the specific dopant site. Comparing the three series, the calcium apatites proved superior with a high ionic conductivity of 3.44×10^{-4} S cm^{-1} ($x = 0.5$) at 500 °C and a relatively low activation energy (E_a) of 0.95 eV (Table 4).

4. Discussion

Bond valence summing (BVS) for each cation in the Sr substituted $[A^I_4][A^{II}_6][(BO_4)_6][O_2]$ system[53,54] (Table S10†) was used to validate metal distribution over the polyhedra, with large deviations from formal valence indicative of unsuitable sites. Moreover, BVS can probe the relative occupancy numbers of disordered sites and detect lattice strain. As expected, the calculated BVS shows La^{3+} and V^{5+} to be underbonded and those for Sr^{2+} and Ge^{4+} overbonded, but the average BVS for A^I and B sites is close to ideal with 2.45/2.51 and 4.13/4.07 (AE = Sr, x = 0.5; bond lengths refined from neutron diffraction).

The metaprism twist angles (φ) for the Ca and Sr series are well below an upper limit ~25°, beyond which hexagonal symmetry cannot sustain acceptable bond valence sum limits without rotation of the tetrahedra.[55,56] Typically, at larger metaprism twist angles, apatites metrically distort from hexagonal $P6_3/m$ symmetry to monoclinic $P2_1/m$ or triclinic $P\bar{1}$ with a diminution of oxygen mobility. Since φ for the Ba-series is near the phase transition, this offers a partial explanation for the low conductivity.

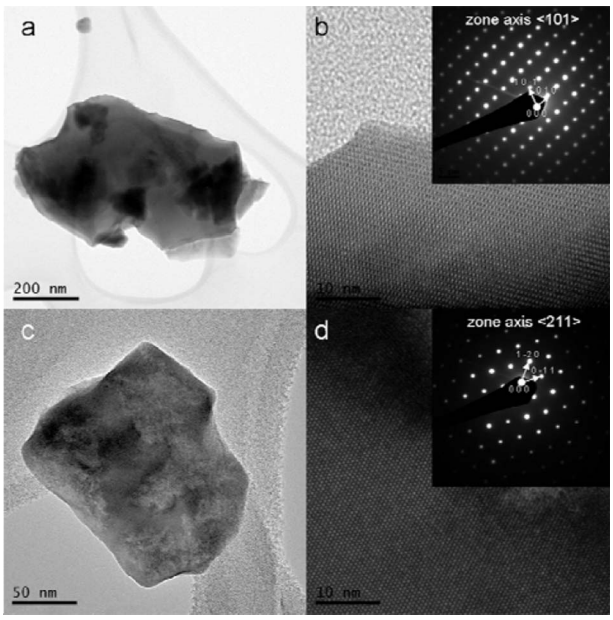

Fig. 7 TEM images (low-magnification and high-resolution) and diffraction patterns for nominal (a and b) $[La_8Sr_2][Ge_6]O_{26}$ and (c and d) $[La_8Sr_2][Ge_{5.5}V_{0.5}]O_{26.25}$.

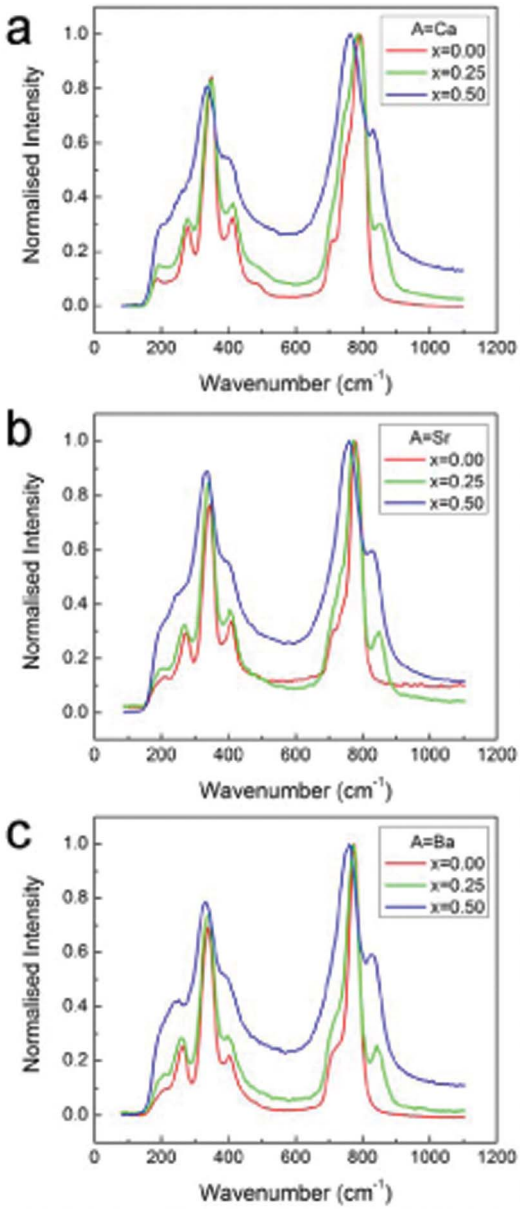

Fig. 8 Raman spectra of normalised intensities for (a) $La_8Ca_2Ge_{6-x}V_xO_{26+x/2}$, (b) $La_8Sr_2Ge_{6-x}V_xO_{26+x/2}$, and (c) $La_8Ba_2Ge_{6-x}V_xO_{26+x/2}$ series with nominal x = 0, 0.25, and 0.5, measured at room temperature.

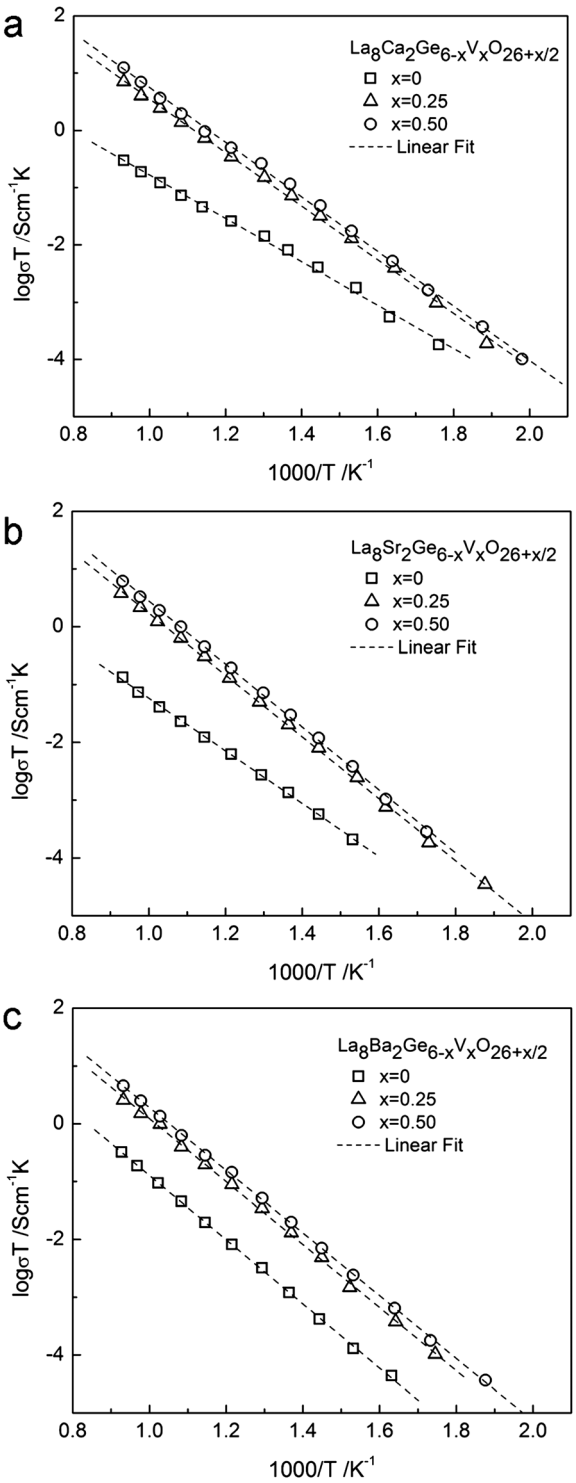

Fig. 9 Variation of conductivities with temperatures for (a) $La_8Ca_2Ge_{6-x}V_xO_{26+x/2}$, (b) $La_8Sr_2Ge_{6-x}V_xO_{26+x/2}$, and (c) $La_8Ba_2Ge_{6-x}V_xO_{26+x/2}$ series with nominal $x = 0$, 0.25, and 0.5.

The introduction of vanadium generally increases the total oxygen content (mechanism (2) dominant), although some oxygen-deficient apatites appear due to the creation of La^{3+} cation vacancies (mechanism (3) dominant). Superstoichiometric oxygen facilitates an interstitial conducting mechanism,[2,12,25,57]

Table 4 Conductivity data for $La_8AE_2Ge_{6-x}V_xO_{26+x/2}$ (AE = Ca, Sr, Ba; $0 \leq x \leq 0.5$) samples

Apatite (nominal composition)	Density of pellet (% theoretical)	σ at 500 °C/ S cm^{-1}	E_a/eV
$La_8Ca_2Ge_6O_{26}$	84	1.84×10^{-5}	0.75
$La_8Ca_2Ge_{5.75}V_{0.25}O_{26.125}$	86	1.97×10^{-4}	0.93
$La_8Ca_2Ge_{5.5}V_{0.5}O_{26.25}$	93	3.44×10^{-4}	0.95
$La_8Sr_2Ge_6O_{26}$	81	3.53×10^{-6}	0.91
$La_8Sr_2Ge_{5.75}V_{0.25}O_{26.125}$	97	6.49×10^{-5}	1.06
$La_8Sr_2Ge_{5.5}V_{0.5}O_{26.25}$	97	9.39×10^{-5}	1.08
$La_8Ba_2Ge_6O_{26}$	92	4.16×10^{-6}	1.10
$La_8Ba_2Ge_{5.75}V_{0.25}O_{26.125}$	94	4.45×10^{-5}	1.08
$La_8Ba_2Ge_{5.5}V_{0.5}O_{26.25}$	97	6.68×10^{-5}	1.08

and cation vacancies located at 4*f* sites could cause 2*a* O^{2-} ion displacement and creation of "interstitial-like" positions, which provide favourable diffusion paths across and through the tunnels.[8,10,13] The variable vacancy concentration makes the evaluation of conductivities with increasing x more complex, although the evolution of conductivity correlates with the relative proportions of oxygen interstitials and cation vacancies. Specifically, oxygen nonstoichiometry, conductivity, and activity energy can be rationalised when plotted against the metaprism twist angle (Fig. 4d–f). In general, the Ca series displays opposite trends compared to the Ba and Sr series because $Ca^{2+} < La^{3+}$ while Sr^{2+}, $Ba^{2+} > La^{3+}$ with respect to the ionic size. Most obviously, ionic conductivity correlates well with the oxygen nonstoichiometry, with σ generally increasing with greater oxygen stoichiometry. Comparing the three analogues, the conductivity decreased in the order Ca > Sr > Ba following the observations of Pramana *et al.*[58] for the alkaline earth lanthanum germanate oxyapatite; this behaviour is contrary to the silicate apatites where Ba-doped apatites were superior.[5] The lowest activation energies arise when the large tunnel is greatly expanded (φ small) that facilitates oxygen migration with the trend across the three analogues following the order Ca < Sr < Ba. Besides intrinsic factors, several extrinsic properties influence conductivity, especially porosity, grain size and crystal habit. For example, grain morphology is compositionally dependent: the calcium-doped series have isotropic grains, while the strontium and barium series are acicular crystals with the largest $c : a$ aspect ratios observed for the latter. Moreover, vanadium not only causes crystal chemical changes, but also promotes phase and microstructural changes. For example, amorphous material is less abundant in vanadium doped products indicative of better crystallisation, although the crystals were more anisotropic. As conductivity along the *c* axis is much larger than that along the *a* axis,[3] textural modification of the compact pellets would influence bulk conductivities. Although there was no evidence of severe textural phenomena in the pellets as observed in the EBSD map, clusters of crystals showing preferred orientation could exist in local areas.

5. Conclusion

Three series of vanadium doped electrolyte apatites with nominal composition $[La_8AE_2][Ge_{6-x}V_x]O_{26+x/2}$ (AE = Ca, Sr, Ba; $0 \leq x \leq 1.5$) were synthesised and characterised by laboratory X-ray, synchrotron and neutron diffraction followed by Rietveld

refinement. The chemical compositions, microstructures, and local structures were analysed by SEM and TEM. Single-phase apatites were obtained for nominal $x \leq 0.5$ and structural investigations were invariably consistent with $P6_3/m$ symmetry. All the three series show an order of magnitude enhancement in conductivity, even with low-level vanadium doping; the best performance was for the calcium doped series. The conductivities and activation energy are controlled by dopant size, melting temperature, crystallinity, and the microstructure of the sintered pellets. Compositions with $AE = Sr$, $x > 0$ and $AE = Ba$, $x \geq 0$ show particularly strong anisotropic grain growth, and therefore their conductive properties are likely to be texturally limited. Overall, the vanadium-doped apatites show potential as electrolytes for intermediate temperature SOFCs, with $\sigma = 3.44 \times 10^{-4}$ S cm^{-1} at 500 °C and a relatively low activation energy (0.95 eV) achieved.

For these apatite electrolytes, crystallochemical tailoring to enhance performance confirmed four general principles:

(a) *Smaller A^IO_6 metaprism twist angles open the channel to promote conductivity*. Consequently, the Ca series shows the greatest oxygen mobility, as the smaller average ionic size of the framework cations reduces twisting and enlarges the tunnel diameter. In addition, φ is well below 25°, beyond which lower symmetries are favoured that create more intricate ion migration paths and reduce conductivity.

(b) *Excess oxygen allows interstitial mobility, leading to higher conductivity*. The introduction of V^{5+} in Ge^{4+} is offset by the incorporation of superstoichiometric oxygen that leads to greater σ at intermediate temperatures.

(c) *Activation energy is lower in expanded tunnels*, where the barriers to ion migration are more easily overcome. Therefore, compositional series with smaller φ and enlarged tunnel are generally preferred.

(d) *Superstoichiometric oxygen may be ordered or disordered*. In $La_{10}(GeO_4)_5(GeO_5)O_2$ perfect correlation of superstoichiometric oxygen was observed.[18] However, in the materials studied here there is no direct evidence for interstitial sites, but the cation contents derived from structure refinement require O^{2-} for charge balance.

Acknowledgements

The author H. Li acknowledges the Nanyang President's Graduate Scholarship (NPGS) provided by Nanyang Technological University. This work was supported by A*STAR (Agency for Science, Technology and Research) SERC Grant 082 101 0021 "Optimization of Apatite Anion Sublattices in Solid Oxide Fuel Cell Electrolytes".

Reference

1 S. Nakayama, H. Aono and Y. Sadaoka, *Chem. Lett.*, 1995, **24**, 431–432.
2 S. Nakayama and M. Sakamoto, *J. Eur. Ceram. Soc.*, 1998, **18**, 1413–1418.
3 S. Nakayama, M. Sakamoto, M. Higuchi, K. Kodaira, M. Sato, S. Kakita, T. Suzuki and K. Itoh, *J. Eur. Ceram. Soc.*, 1999, **19**, 507–510.
4 H. Arikawa, H. Nishiguchi, T. Ishihara and Y. Takita, *Solid State Ionics*, 2000, **136–137**, 31–37.
5 S. Beaudet-Savignat, A. Vincent, S. Lambert and F. Gervais, *J. Mater. Chem.*, 2007, **17**, 2078–2087.
6 P. Berastegui, S. Hull, F. J. GarcI GarcI and J. Grins, *J. Solid State Chem.*, 2002, **168**, 294–305.
7 A. Chesnaud, G. Dezanneau, C. Estournès, C. Bogicevic, F. Karolak, S. Geiger and G. Geneste, *Solid State Ionics*, 2008, **179**, 1929–1939.
8 E. Kendrick, M. S. Islam and P. R. Slater, *J. Mater. Chem.*, 2007, **17**, 3104–3111.
9 E. Kendrick, M. S. Islam and P. R. Slater, *Solid State Ionics*, 2007, **177**, 3411–3416.
10 E. Kendrick, M. S. Islam and P. R. Slater, *Chem. Commun.*, 2008, 715–717.
11 V. V. Kharton, F. M. B. Marques and A. Atkinson, *Solid State Ionics*, 2004, **174**, 135–149.
12 V. V. Kharton, A. L. Shaula, M. V. Patrakeev, J. C. Waerenborgh, D. P. Rojas, N. P. Vyshatko, E. V. Tsipis, A. A. Yaremchenko and F. M. B. Marques, *J. Electrochem. Soc.*, 2004, **151**, A1236–A1246.
13 L. Leon-Reina, E. R. Losilla, M. Martinez-Lara, S. Bruque, A. Llobet, D. V. Sheptyakov and M. A. G. Aranda, *J. Mater. Chem.*, 2005, **15**, 2489–2498.
14 L. Leon-Reina, M. C. Martin-Sedeno, E. R. Losilla, A. Cabeza, M. Martinez-Lara, S. Bruque, F. M. B. Marques, D. V. Sheptyakov and M. A. G. Aranda, *Chem. Mater.*, 2003, **15**, 2099–2108.
15 L. Leon-Reina, J. M. Porras-Vazquez, E. R. Losilla and M. A. G. Aranda, *Solid State Ionics*, 2006, **177**, 1307–1315.
16 S. Nakayama and M. Highchi, *J. Mater. Sci. Lett.*, 2001, **20**, 913–915.
17 S. Nakayama and M. Sakamoto, *J. Mater. Sci. Lett.*, 2001, **20**, 1627–1629.
18 S. S. Pramana, W. T. Klooster and T. J. White, *Acta Crystallogr., Sect. B: Struct. Sci.*, 2007, **63**, 597–602.
19 S. S. Pramana, W. T. Klooster and T. J. White, *J. Solid State Chem.*, 2008, **181**, 1717–1722.
20 J. E. H. Sansom, D. Apperley and P. R. Slater, *J. Mater. Chem.*, 2006, **16**, 1410–1413.
21 J. E. H. Sansom, L. Hildebrandt and P. R. Slater, *Ionics*, 2002, **8**, 155–160.
22 J. E. H. Sansom and P. R. Slater, *Diffus. Defect Data, Pt. B*, 2003, **90–91**, 189–194.
23 A. L. Shaula, V. V. Kharton, J. C. Waerenborgh, D. P. Rojas and F. M. B. Marques, *J. Eur. Ceram. Soc.*, 2005, **25**, 2583–2586.
24 P. R. Slater, J. E. H. Sansom and J. R. Tolchard, *Chem. Rec.*, 2004, **4**, 373–384.
25 J. R. Tolchard, M. S. Islam and P. R. Slater, *J. Mater. Chem.*, 2003, **13**, 1956–1961.
26 J. R. Tolchard, P. R. Slater and M. S. Islam, *Adv. Funct. Mater.*, 2007, **17**, 2564–2571.
27 T. J. White and Z. Dong, *Acta Crystallogr., Sect. B: Struct. Sci.*, 2003, **59**, 1–16.
28 J. E. H. Sansom, D. Richings and P. R. Slater, *Solid State Ionics*, 2001, **139**, 205–210.
29 P. R. Slater and J. E. H. Samson, *Diffus. Defect Data, Pt. B*, 2003, **90–91**, 195–200.
30 M. S. Islam, J. R. Tolchard and P. R. Slater, *Chem. Commun.*, 2003, 1486–1487.
31 H. Yoshioka and S. Tanase, *Solid State Ionics*, 2005, **176**, 2395–2398.
32 A. Najib, J. E. H. Sansom, J. R. Tolchard, P. R. Slater and M. S. Islam, *Dalton Trans.*, 2004, 3106–3109.
33 G.-L. Wang, M.-L. Zhang, H. Zhao, L.-H. Huo and L.-P. Sun, *Wuji Cailiao Xuebao*, 2006, **21**, 1258–1262.
34 W. Yuan, R. Shen and L. Li, *Chin. J. Chem. Eng.*, 2010, **18**, 328–332.
35 Bruker, Topas version 4.1, Bruker AXS Inc., Madison, Wisconsin, USA, 2008.
36 H. Yoshioka, *J. Alloys Compd.*, 2006, **408–412**, 649–652.
37 V. F. Sears, *Neutron News*, 1992, **3**, 26–37.
38 E. J. Abram, C. A. Kirk, D. C. Sinclair and A. R. West, *Solid State Ionics*, 2005, **176**, 1941–1947.
39 L. Suo Hon, C. Ritter, P. Yang, M. Schreyer and T. J. White, *J. Appl. Crystallogr.*, 2009, **42**, 917–924.
40 R. D. Shannon, *Acta Crystallogr., Sect. A: Cryst. Phys., Diffr., Theor. Gen. Crystallogr.*, 1976, **32**, 751–767.
41 Y. Masubuchi, M. Higuchi, T. Takeda and S. Kikkawa, *Solid State Ionics*, 2006, **177**, 263–268.
42 F. J. Humphreys and M. Hatherly, *Recrystallization and Related Annealing Phenomena*, Elsevier, 2004.

43 S. Nishiwaki, J. Takahashi and K. Kodaira, *Jpn. J. Appl. Phys.*, 1994, **33**, 5477–5481.
44 A. Y. Oral and M. L. Mecartney, *J. Mater. Sci.*, 2001, **36**, 5519–5527.
45 Z. L. Dong, T. J. White, K. Sun, L. M. Wang and R. C. Ewing, *J. Am. Ceram. Soc.*, 2005, **88**, 184–190.
46 E. Rodríguez-Reyna, A. F. Fuentes, M. Maczka, J. Hanuza, K. Boulahya and U. Amador, *Solid State Sci.*, 2006, **8**, 168–177.
47 A. Orera, M. L. Sanjuan, E. Kendrick, V. M. Orera and P. R. Slater, *J. Mater. Chem.*, 2010, 20, 2170–2175.
48 S.-H. Lee, H. M. Cheong, M. J. Seong, P. Liu, C. E. Tracy, A. Mascarenhas, J. R. Pitts and S. K. Deb, *Solid State Ionics*, 2003, **165**, 111–116.
49 C. Julien, G. A. Nazri and O. Bergstroem, *Phys. Status Solidi B*, 1997, **201**, 319–326.
50 C. B. Boechat, J. Terra, J.-G. Eon, D. E. Ellis and A. M. Rossi, *Phys. Chem. Chem. Phys.*, 2003, **5**, 4290–4298.
51 F. A. Settle, *Handbook of Instrumental Techniques for Analytical Chemistry*, Prentice Hall PTR, Upper Saddle River, NJ, 1997.
52 E. Kendrick and P. R. Slater, *Solid State Ionics*, 2008, **179**, 981–984.
53 I. D. Brown and D. Altermatt, *Acta Crystallogr., Sect. B: Struct. Sci.*, 1985, **41**, 244–247.
54 N. E. Brese and M. O'Keeffe, *Acta Crystallogr., Sect. B: Struct. Sci.*, 1991, **47**, 192–197.
55 T. Baikie, P. H. J. Mercier, M. M. Elcombe, J. Y. Kim, Y. Le Page, L. D. Mitchell, T. J. White and P. S. Whitfield, *Acta Crystallogr., Sect. B: Struct. Sci.*, 2007, **63**, 251–256.
56 P. S. Whitfield, Y. Le Page, P. H. J. Mercier and J. Y. Kim, *J. Appl. Crystallogr.*, 2007, **40**, 1019–1026.
57 S. W. Tao and J. T. S. Irvine, *Mater. Res. Bull.*, 2001, **36**, 1245–1258.
58 S. S. Pramana, T. Baikie, E. Kendrick, M. K. Schreyer, P. R. Slater and T. J. White, *Solid State Ionics*, 2010, **181**, 1189–1196.